

# Using Frequent, High-Resolution Remote Sensing to Identify Intermittent and Overlapping CH<sub>4</sub> sources in Oil and Gas Development Regions

Matthew Alvarado<sup>1</sup>, Archana Dayalu<sup>1</sup>, David B Hogan<sup>1</sup>, Igor Polonsky<sup>1</sup>, Gary Start<sup>2</sup>, Philip Father<sup>2</sup>, Sam Aminfar<sup>3</sup>, Felipe J Cardoso-Saldaña<sup>4</sup>, and Cynthia A Randles<sup>5</sup>

<sup>1</sup>AER

<sup>2</sup>Scepter

<sup>3</sup>ExxonMobil Upstream Research Company

<sup>4</sup>ExxonMobil Technology and Engineering

<sup>5</sup>ExxonMobil Research and Engineering Company

April 29, 2023

## Abstract

The oil and natural gas industry needs accurate and frequent information on methane CH<sub>4</sub> emissions from all of their facilities globally in order to effectively reduce emissions. Here we describe the development of requirements for a constellation of satellites to provide frequent data on point source CH<sub>4</sub> emissions from the oil and gas industry. Three types of sources were examined: isolated continuous plumes with emissions rates of 50 kg hr<sup>-1</sup>, intermittent CH<sub>4</sub> releases from activities such as compressor start-ups, and overlapping continuous plumes. The dispersion model SCICHEM was used to simulate the dispersion of methane plumes and intermittent releases for typical meteorology in the Permian Basin, and a plume mask and integrated mass enhancement (IME) algorithm were applied to identify and quantify the emissions. The precision and ground sampling distance of the future satellite instrument were varied to determine the required precision and horizontal resolution of the satellite instrument. We find that quantifying CH<sub>4</sub> point source emissions as small as 50 kg hr<sup>-1</sup> by remote sensing requires a ground sampling distance of 30-60 m and a CH<sub>4</sub> column precision of 0.5-1.0% for the range of conditions analyzed. Detecting intermittent sources is also possible with the above instrument specifications if the puff is observed within 15 min of emission. Plumes of similar source strengths more than 0.5 km apart can be separated with existing plume identification approaches but separating sources closer than that or with very different emission rates will require further development of plume identification techniques.

## Hosted file

961320\_0\_art\_file\_10903029\_rt9jzl.docx available at <https://authorea.com/users/609071/articles/638653-using-frequent-high-resolution-remote-sensing-to-identify-intermittent-and-overlapping-ch4-sources-in-oil-and-gas-development-regions>

## Hosted file

961320\_0\_supp\_10902950\_rt9jqk.docx available at <https://authorea.com/users/609071/articles/638653-using-frequent-high-resolution-remote-sensing-to-identify-intermittent-and-overlapping-ch4-sources-in-oil-and-gas-development-regions>

1  
2 **Using Frequent, High-Resolution Remote Sensing to Identify Intermittent and**  
3 **Overlapping CH<sub>4</sub> sources in Oil and Gas Development Regions**

4 **M. J. Alvarado<sup>1</sup>, A. Dayalu<sup>1</sup>, D. B. Hogan<sup>1</sup>, I. N. Polonsky<sup>1</sup>, G. Start<sup>2</sup>, P. Father<sup>2</sup>, S.**  
5 **Aminfard<sup>3</sup>, F. J. Cardoso-Saldaña<sup>3</sup>, and C. A. Randles<sup>4,5</sup>**

6  
7  
8 <sup>1</sup>Verisk Atmospheric and Environmental Research, Lexington, MA.

9 <sup>2</sup>Scepter, San Francisco, CA.

10 <sup>3</sup>ExxonMobil Technology and Engineering, Houston, TX.

11 <sup>4</sup>ExxonMobil Research and Engineering, Annandale, NJ.

12 <sup>5</sup>Now at United Nations Environment Program's International Methane Emissions Observatory,  
13 Paris, France.

14  
15 Corresponding author: Matthew J. Alvarado ([malvarad@aer.com](mailto:malvarad@aer.com))

16 **Key Points:**

- 17 • Quantifying CH<sub>4</sub> point source emissions as small as 50 kg hr<sup>-1</sup> requires a ground  
18 resolution of 30-60 m and a column precision of 0.5-1.0%.
- 19 • Detecting intermittent sources with the above specifications is possible if the puff is  
20 observed within 15 min of emission.
- 21 • Plumes of similar source strengths within less than 0.5 km of each other will be difficult  
22 to separate in remote sensing observations.

## 23 **Abstract**

24 The oil and natural gas industry needs accurate and frequent information on methane CH<sub>4</sub>  
25 emissions from all of their facilities globally in order to effectively reduce emissions. Here we  
26 describe the development of requirements for a constellation of satellites to provide frequent data  
27 on point source CH<sub>4</sub> emissions from the oil and gas industry. Three types of sources were  
28 examined: isolated continuous plumes with emissions rates of 50 kg hr<sup>-1</sup>, intermittent CH<sub>4</sub>  
29 releases from activities such as compressor start-ups, and overlapping continuous plumes. The  
30 dispersion model SCICHEM was used to simulate the dispersion of methane plumes and  
31 intermittent releases for typical meteorology in the Permian Basin, and a plume mask and  
32 integrated mass enhancement (IME) algorithm were applied to identify and quantify the  
33 emissions. The precision and ground sampling distance of the future satellite instrument were  
34 varied to determine the required precision and horizontal resolution of the satellite instrument.  
35 We find that quantifying CH<sub>4</sub> point source emissions as small as 50 kg hr<sup>-1</sup> by remote sensing  
36 requires a ground sampling distance of 30-60 m and a CH<sub>4</sub> column precision of 0.5-1.0% for the  
37 range of conditions analyzed. Detecting intermittent sources is also possible with the above  
38 instrument specifications if the puff is observed within 15 min of emission. Plumes of similar  
39 source strengths more than 0.5 km apart can be separated with existing plume identification  
40 approaches but separating sources closer than that or with very different emission rates will  
41 require further development of plume identification techniques.

## 42 **Plain Language Summary**

43 In order to reduce greenhouse gas emissions from the oil and natural gas industry, and thus  
44 reduce near-term global warming, more frequent and accurate information on which of their  
45 facilities are emitting methane is needed. Satellite observations can help due to their global  
46 coverage, and recent advancements in sensor technology will make it possible to measure up to  
47 80-90% of the methane emissions from the oil and gas industry. In this work we discuss  
48 instrument requirements toward a future group of satellites that will measure methane emissions  
49 from oil and gas facilities multiple times a day. We looked at small, steady sources of methane  
50 and determined that measuring these sources would require a satellite instrument that can  
51 measure methane to within 0.5-1.0% every 30-60 m horizontally. We find that detecting small,  
52 unsteady sources, such as those from starting a natural gas compressor, is also possible, but only  
53 if the source is observed within 15 minutes after the emission. Finally, we show that current  
54 techniques can only separate neighboring sources of CH<sub>4</sub> if they are of similar size and at least  
55 0.5 km apart.

## 56 **1 Introduction**

57 Emissions of methane (CH<sub>4</sub>) to the atmosphere are receiving increased attention as a  
58 method to reduce greenhouse gas radiative forcing and the resulting climatic changes (e.g.,  
59 Nisbet et al., 2020). Reductions of CH<sub>4</sub> emissions are attractive as the relatively short lifetime of  
60 CH<sub>4</sub> in the atmosphere ( $9.1 \pm 0.9$  yr., Szopa et al., 2021) means that changes in CH<sub>4</sub> emissions  
61 could reduce climate forcing over a 10- to 20-year horizon, delaying when a given temperature  
62 threshold will be crossed and allowing for more time to address emissions of the longer-lived  
63 greenhouse gas carbon dioxide (CO<sub>2</sub>).

64 CH<sub>4</sub> emissions come from a wide variety of sources, including natural sources such as  
65 wetlands and wildfires and anthropogenic sources like livestock, rice cultivation, landfills,

66 biofuel burning, and fossil fuel use (e.g., Saunio et al., 2020). Fossil fuel sources of CH<sub>4</sub>  
67 account for about 18% of the annual global CH<sub>4</sub> emissions and include emissions from coal  
68 mining (33% of fossil fuel CH<sub>4</sub> emissions for 2017) and the oil and natural gas industry (62% of  
69 fossil fuel CH<sub>4</sub> emissions for 2017, Saunio et al., 2020).

70 Emissions from oil and gas activities are complex as they are skewed, with a small  
71 number of sources accounting for a large fraction of emissions (Brandt et al., 2016), and have  
72 spatiotemporal variability (Allen et al., 2017; Cusworth et al., 2021). In recent years, high CH<sub>4</sub>  
73 emissions from oil and gas activities have been observed with aircraft and satellites in the US  
74 and around the world (Cusworth et al., 2021; Cusworth et al., 2022; Lauvaux et al. 2021), and  
75 they account for a disproportionate fraction of total emissions in a given region. For example, in  
76 the Permian basin, close to 90% of total emissions originate from plumes larger than 50 kg/hr  
77 (Chen et al., 2022). In order to achieve significant reductions on emissions, industry needs  
78 emission information in near-real-time for high emitter sources, such that mitigation measures  
79 can be taken to address unexpected CH<sub>4</sub> emissions when they appear (Cardoso-Saldaña 2022). In  
80 addition, the locations of emission sources need to be identified accurately to allow mitigation  
81 activities to be performed, especially as different companies may have emitting equipment  
82 within close proximity to each other. Finally, there is a need to detect intermittent sources of  
83 CH<sub>4</sub>, as persistent emission sources account for only 29% of oil and natural gas industry  
84 emissions in areas like the Permian basin (Cusworth et al., 2021).

85 Providing the information on CH<sub>4</sub> emissions needed by the oil and gas industry will  
86 require a mixture of measurement approaches that combines in situ methane observations with  
87 additional information from ground-based (e.g., Pernini et al., 2022), aircraft (Duren et al., 2019;  
88 Jongaramrungruang et al., 2019; Cusworth et al., 2020), and satellite remote sensing platforms.  
89 Of these platforms, satellite observations are of particular interest due to their ability to observe  
90 methane sources globally.

91 Jacob et al. (2022) recently reviewed satellite methods to quantify methane emissions  
92 from the global scale down to individual point sources. They separated methane monitoring  
93 satellites into two general categories, area flux mappers and point source imagers. Area flux  
94 mappers are designed to observe total emissions on global or regional scales with 0.1–10 km  
95 pixel size (Jacob et al., 2022). These include the European Space Agency TROPospheric  
96 Monitoring Instrument (TROPOMI) instrument, which has been used to detect high-emitting  
97 CH<sub>4</sub> sources in oil and gas fields with a low density of sites (Cusworth et al., 2018). Varon et al.  
98 (2022) created user-friendly, cloud-based facility for quantifying CH<sub>4</sub> emissions with  
99  $0.25^\circ \times 0.3125^\circ$  resolution by inverse analysis of satellite observations from TropOMI.

100 Point source imagers are fine-pixel (< 60 m) instruments designed to quantify individual  
101 point sources by imaging the plumes (Jacob et al., 2022). For example, Varon et al. (2020) used  
102 the GHGSat-D satellite instrument (50 m effective spatial resolution and 9–18% single-pass  
103 column precision) to quantify mean source rates for three coal mine vents (2320 to 5850 kg h<sup>-1</sup>).  
104 Varon et al. (2021) used data from the Sentinel-2 mission to quantify point sources down to  
105 about 3 t h<sup>-1</sup>, with Ehret et al. (2022) using similar methods to detect and quantify more than  
106 1200 CH<sub>4</sub> emissions from Seninel-2 data. Sánchez-García et al. (2022) used data from the  
107 WorldView-3 (WV-3) satellite mission to detect point emissions over oil and gas extraction  
108 fields in Algeria and Turkmenistan.

109           The goal of the Scepter Monitoring Mission is to provide frequent, high-resolution data  
110 on multiple air pollutants to a variety of industrial and government entities. Here we focus on the  
111 development of requirements for a constellation of satellites to provide frequent data on point  
112 source CH<sub>4</sub> emissions from the oil and gas industry. A systems engineering requirement flow-  
113 down process was used to determine the satellite and constellation (~14 satellites) requirements  
114 to measure CH<sub>4</sub> leak rates of 50 kg hr<sup>-1</sup> multiple times a day, thereby meeting the needs of the oil  
115 and gas industry. In this paper, we describe the first step of this process, where the dispersion  
116 model SCICHEM was used to simulate the dispersion of methane plumes during a typical day in  
117 the Permian Basin. The CH<sub>4</sub> emission rates were fixed at 50 kg hr<sup>-1</sup> for different wind speeds and  
118 meteorological conditions and the resulting column enhancements (g m<sup>-2</sup>) were calculated. A  
119 noisy background of CH<sub>4</sub> was added to simulate the satellite observations. Then a plume mask  
120 and integrated mass enhancement (IME) algorithm based on the approach of Varon et al. (2018)  
121 was applied. The value of the noise and the ground sampling distance of the instrument were  
122 varied to determine the required precision and horizontal resolution of the satellite instrument.

123           In addition, this paper focuses on two challenging aspects of monitoring oil and natural  
124 gas industry CH<sub>4</sub> emissions from satellites. First, intermittent, unintentional CH<sub>4</sub> releases need to  
125 be detected and quantified. Cusworth et al. (2022) showed these intermittent sources accounted  
126 for nearly half of the total CH<sub>4</sub> point source budget for multiple basins in the United States. To  
127 study these sources, we performed instantaneous releases in SCICHEM and applied the plume  
128 identification method of Varon et al. (2018) to the resulting puffs.

129           Second, at oil and gas facilities the plumes from multiple sources may overlap, making it  
130 more difficult to separate their emissions. This is less of a challenge for scientific studies that  
131 aim at determining the total CH<sub>4</sub> emission in a given region, as in those studies an accurate total  
132 emission rate is more important than separating the emissions among the individual sources.  
133 However, for our goal of providing information to operators that allow them to quickly address  
134 emissions, separating the emissions from different sources is critical to send staff to the correct  
135 location, as well as to identify which company should respond when the facilities of different  
136 companies are near each other. To address this, we simulated different configurations of  
137 overlapping plumes with the SCICHEM model, applied our plume masking algorithm, and  
138 examined how difficult it would be to separate the plumes under different wind directions,  
139 source strengths, and inter-plume distances.

## 140 2 Methods

### 141 2.1 Satellite Instrument Performance

142 We assumed a future satellite instrument operating in the 2050-2400  $\mu\text{m}$  band with a  
 143 signal to noise ratio (SNR) between 100-150, a spectral resolution between 1- 5 nm, and a  
 144 ground sampling distance between 30-120 m. These specifications are well within the limits of  
 145 current technology. We calculated the expected variance ( $\sigma$ ) reduction due to adding a  
 146 measurement to a system described by a prior information following Rodgers (2000):

$$\sigma^{-1} = K^T \left( \frac{SNR}{y} \right)^2 K + S_a^{-1}$$

147 where  $y$  is the measured radiance,  $K$  is the Jacobian (sensitivity of the radiance to changes in the  
 148  $\text{CH}_4$  profile),  $SNR$  is the signal to noise ratio, and  $S_a$  is the prior covariance matrix. The  
 149 Jacobians were computed using LBLRTM v12.13 (Clough et al., 2005, Alvarado et al., 2013)  
 150 based on the finite difference method using a surface albedo of 0.15, which is less than the 25<sup>th</sup>  
 151 percentile of surface albedo values in the Permian basin year-round. As we are interested in  
 152 detecting near-surface enhancements of  $\text{CH}_4$ , the prior covariance was calculated assuming that  
 153 the 1-sigma uncertainty in the  $\text{CH}_4$  concentration in the planetary boundary layer was about 10%  
 154 of the total column.

155 For an instrument with a SNR between 100-150 and a spectral resolution between 1- 5  
 156 nm, the above procedure estimated a  $\text{CH}_4$  column precision of between 0.3-1.0%. However, this  
 157 procedure does not account for the potential impacts of errors in other retrieved species (mainly  
 158  $\text{H}_2\text{O}$  and surface reflectance) on the retrieved  $\text{CH}_4$  precision. Thus, for the plume identification  
 159 and quantification studies below, we assumed a more conservative error range of 0.5-1.0%.

### 160 2.2 SCICHEM Dispersion Modeling

161 We used the SCICHEM dispersion model to simulate both continuous and instantaneous releases  
 162 of  $\text{CH}_4$ . Hourly surface meteorological data were obtained from the Pine Springs, Guadalupe  
 163 Mountains National Park (KGDP) weather station (31.83 °N, 104.81 °W) and upper air  
 164 meteorological data was obtained from the Midland, TX station (WBAN 23023, 31.93 °N, 102.2  
 165 °W). The SCICHEM preprocessor METSCI was used to prepare the meteorological inputs, with  
 166 the terrain preprocessor TERSCI used to simulate the terrain based on digital elevation model  
 167 (DEM) data. Concentrations were calculated within a horizontal domain of 1 km with a spatial  
 168 resolution of 30 m, and a vertical domain between 0-3 km agl at a vertical resolution of 25 m in  
 169 the lowest 1 km and a 1 km resolution above. We determined the vertical resolution through  
 170 initial SCICHEM runs (not shown) that demonstrated that the non-buoyant  $\text{CH}_4$  emissions  
 171 examined here rarely extended above 1 km in altitude before leaving the 1 km horizontal  
 172 domain, but that a vertical resolution of greater than 25 m in the lowest 1 km led to > 0.1% errors  
 173 in the calculated  $\text{CH}_4$  column. We assumed a stack temperature of 30 °C and a stack exit velocity  
 174 of 0.5  $\text{m s}^{-1}$ , giving the plumes negligible buoyancy.  $\text{CH}_4$  emissions from flares and compressor  
 175 exhaust can be buoyant, but since the satellite measures vertically integrated  $\text{CH}_4$  columns we  
 176 expect the effects of buoyancy on our results to be minimal. We also expect most sources to be

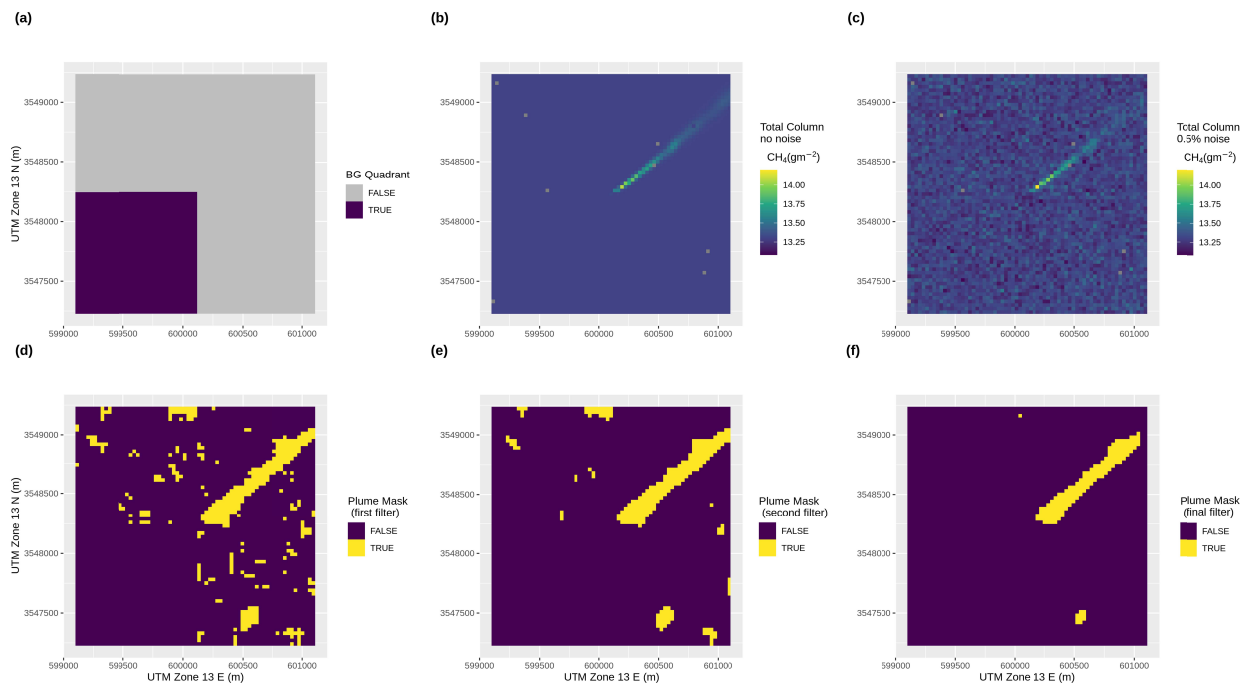
177 near the surface, so the release height and release diameter were both set to 1 m. The CH<sub>4</sub>  
 178 column enhancement was calculated as the vertical integral of the resulting CH<sub>4</sub> profiles.

179 Continuous release simulations were performed in the Permian for a number of different  
 180 wind speeds. Our simulations covered one day (March 8, 2016) with a constant release rate of 50  
 181 kg hr<sup>-1</sup>. We simulated a release at 32.065984 °N, -103.93936 °W, which is the location of Plume  
 182 ID P00203 from the JPL Methane Plume Finder. SCICHEM was also used to simulate an  
 183 instantaneous (<< 1 min) release of 33.5 kg of CH<sub>4</sub> at this location and date. The total emissions  
 184 are roughly the median amount for a compressor blow-down and on the lower end of the range  
 185 for a compressor start-up (Zimmerle et al., 2022) or liquid unloadings (e.g., Allen et al., 2015).

### 186 2.3 Plume Identification and Quantification

187 Our approach for identifying CH<sub>4</sub> plumes and quantifying CH<sub>4</sub> emission rates followed  
 188 the integrated mass enhancement (IME) approach of Varon et al. (2018). The SCICHEM  
 189 simulated column enhancement (Figure 1b) was added to a constant CH<sub>4</sub> background with 0.5%  
 190 or 1% Gaussian noise applied (Figure 1c). The mean background column was set to 13.3 g m<sup>-2</sup>,  
 191 consistent with a background surface concentration of 2000 ppbv. The background CH<sub>4</sub> column  
 192 distribution was then estimated using the up-wind quadrant of the 1 km modeling domain (Figure  
 193 1a).

194 The plume identification algorithm starts by performing a t-test to determine if the  
 195 distribution of CH<sub>4</sub> columns in the 5x5 neighborhood of pixels around a given pixel is  
 196 significantly different (95% confidence) from the background distribution. If so, the center pixel  
 197 is tentatively marked as a plume pixel (Figure 1d). A median 3x3 filter is then applied to the  
 198 resulting t-test mask to remove isolated pixels (Figure 1e), and then a Gaussian filter is applied to  
 199 further remove spurious plume pixels (Figure 1f).



200

201 **Figure 1. (a) Quadrant used to calculate mean and standard deviation of the background**  
 202 **distribution. (b) Simulated plume from a point source of CH<sub>4</sub> with an emission rate of 50**  
 203 **kg hr<sup>-1</sup>. (c) Addition of noisy background (13.3 g m<sup>-2</sup> ± 0.5%). (d) Result of t-test plume**  
 204 **identification. (e) Result of applying the median filter on (d). (f) Result of applying the**  
 205 **Gaussian filter on (e).**

206 Once the plume pixels have been identified, the *IME* (g CH<sub>4</sub>) is defined as the area-  
 207 weighted sum of the column enhancement of methane above background (Figure 2), following  
 208 the equation

$$209 \quad IME = \sum_{pixel=1}^{N_{pixel}} (\Omega_{CH_4, pixel} - \Omega_b) A_{pixel} \quad (1)$$

210 where

- 211 •  $\Omega_{CH_4, pixel}$  is the measured methane column for a single pixel from the Level 2  
 212 product converted to units of g m<sup>-2</sup>
- 213 •  $\Omega_b$  is the background methane column in units of g m<sup>-2</sup> estimated as discussed  
 214 below
- 215 •  $A_{pixel}$  is the area of the pixel in units of m<sup>2</sup>
- 216 •  $N_{pixel}$  is the number of pixels in a single plume

217 The *IME* is combined with the effective plume length:

$$218 \quad L_{eff} = \sqrt{A_{plume}} = \sqrt{\sum_{pixel=1}^{N_{pixel}} A_{pixel}} \quad (2)$$

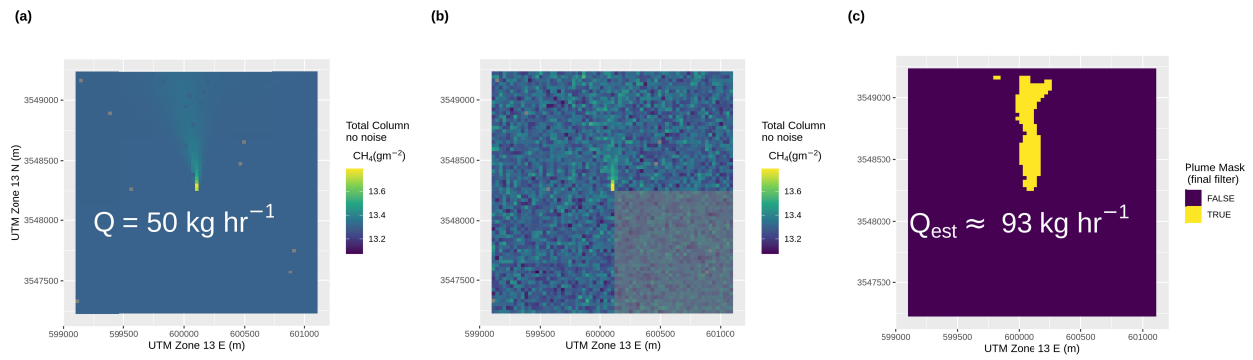
219 and an effective wind speed  $U_{eff}$  (m/s) to estimate the emission rate ( $Q$ , g/s) via the equation:

$$220 \quad Q = \frac{U_{eff}}{L_{eff}} IME \quad (3)$$

221  $U_{eff}$  is calculated from the 10-m wind speed  $U_{10}$  using an equation of the form (Varon et  
 222 al., 2018):

$$223 \quad U_{eff} = a \log U_{10} + b \quad (4)$$

224 Varon et al. (2018) used  $a = 0.9$  and  $b = 0.6$  m s<sup>-1</sup>, and we use the same values for our  
 225 continuous release tests.



226

227 **Figure 2. (a) Simulated plume from a point source of CH<sub>4</sub> with an emission rate of 50 kg hr<sup>-1</sup>**  
 228 **and  $U_{10}$  wind speed of 2.6 m s<sup>-1</sup> at 16 UTC on March 8, 2016. (b) Addition of noisy**  
 229 **background ( $13.3 \text{ g m}^{-2} \pm 0.5\%$ ). (c) Final plume mask and estimated emission rate.**

## 230 2.4 Overlapping Continuous Sources

231 To simulate overlapping continuous sources, we took the simulation shown in Figure 2  
232 and added a second source to the east at distances of 0.25, 0.5, and 0.75 km. The wind direction  
233 for the two plumes were rotated, such that a wind direction of  $0^\circ$  simulated the wind being  
234 perpendicular to the line connecting the point sources and thus has the least overlap, while a  
235 wind direction of  $90^\circ$  has the wind parallel to the line connecting the sources and thus has the  
236 most overlap. We also simulated the intermediate case of  $45^\circ$ . Two cases were simulated for  
237 emission rates, one where both sources had an emission rate of  $50 \text{ kg hr}^{-1}$ , and one where the  
238 western source has a much larger release rate of  $500 \text{ kg hr}^{-1}$  while the eastern source remains at  
239  $50 \text{ kg hr}^{-1}$ .

## 240 3 Results

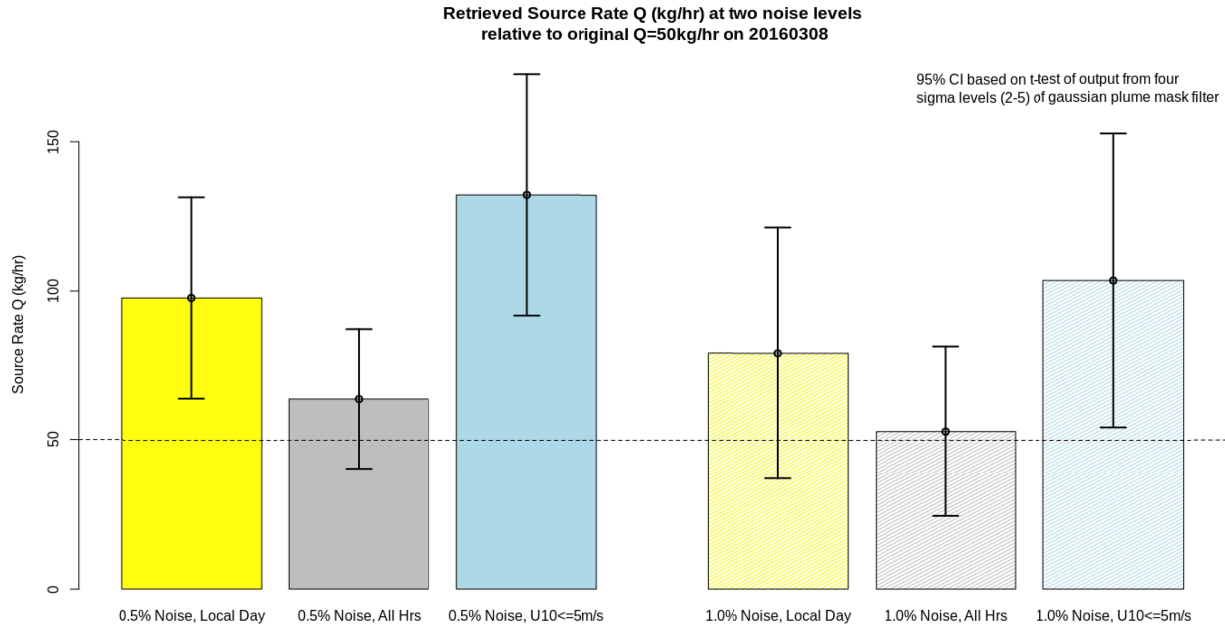
### 241 3.1 Continuous Sources

242 Figure 2 shows the plume mask results for a fairly dispersive plume under low wind  
243 speed conditions ( $2.6 \text{ m s}^{-1}$ ) and an instrument precision of 0.5%. The plume mask for this case  
244 does identify the central core of the plume but is too conservative to identify the full extent of the  
245 plume. This suggests that there is room for improvement in the plume identification algorithm.

246 The retrieved emissions for the true  $50 \text{ kg hr}^{-1}$  rate vary between  $25\text{-}200 \text{ kg hr}^{-1}$  for the 24  
247 hours (and thus 24 meteorological conditions) simulated. Figure 3 shows the mean estimated  
248 source rates for daytime hours (yellow bars), all hours (grey bars), and only hours with wind  
249 speed less than  $5 \text{ m s}^{-1}$  (blue bars) when 0.5% or 1.0% noise is added to the  $\text{CH}_4$  background  
250 column. When data from all hours are averaged, the IME approach used here returns estimates  
251 with small positive biases ( $5\text{-}20 \text{ kg hr}^{-1}$ ). However, our assumed satellite instrument will only be  
252 able to make measurements in the daytime. Looking at only daytime hours leads to a positive  
253 bias of  $25\text{-}50 \text{ kg hr}^{-1}$ . The difference between the all-hours cases and the daylight-hours cases is  
254 that the all-hours cases include more cases with a stable atmosphere, suppressing vertical mixing.

255 Somewhat surprisingly, the higher noise case tends to have a lower positive bias. We  
256 believe this is a case of compensating errors: the positive bias comes from our  $U_{eff}$   
257 parameterization, but the higher noise level leads to an underestimate of the plume extent, and  
258 thus IME, reducing the high noise bias.

259 The positive bias increases further ( $50\text{-}75 \text{ kg hr}^{-1}$ ) if only hours with wind speeds below  $5$   
260  $\text{m s}^{-1}$  are considered. As the plume mask tends to miss plume pixels, it is unlikely that the source  
261 of this bias is the plume mask or the IME calculation, which suggested that addressing these  
262 biases requires further refinement of the  $U_{eff}$  parameterization, potentially to include other  
263 meteorological inputs than just  $U_{10}$  wind speed.

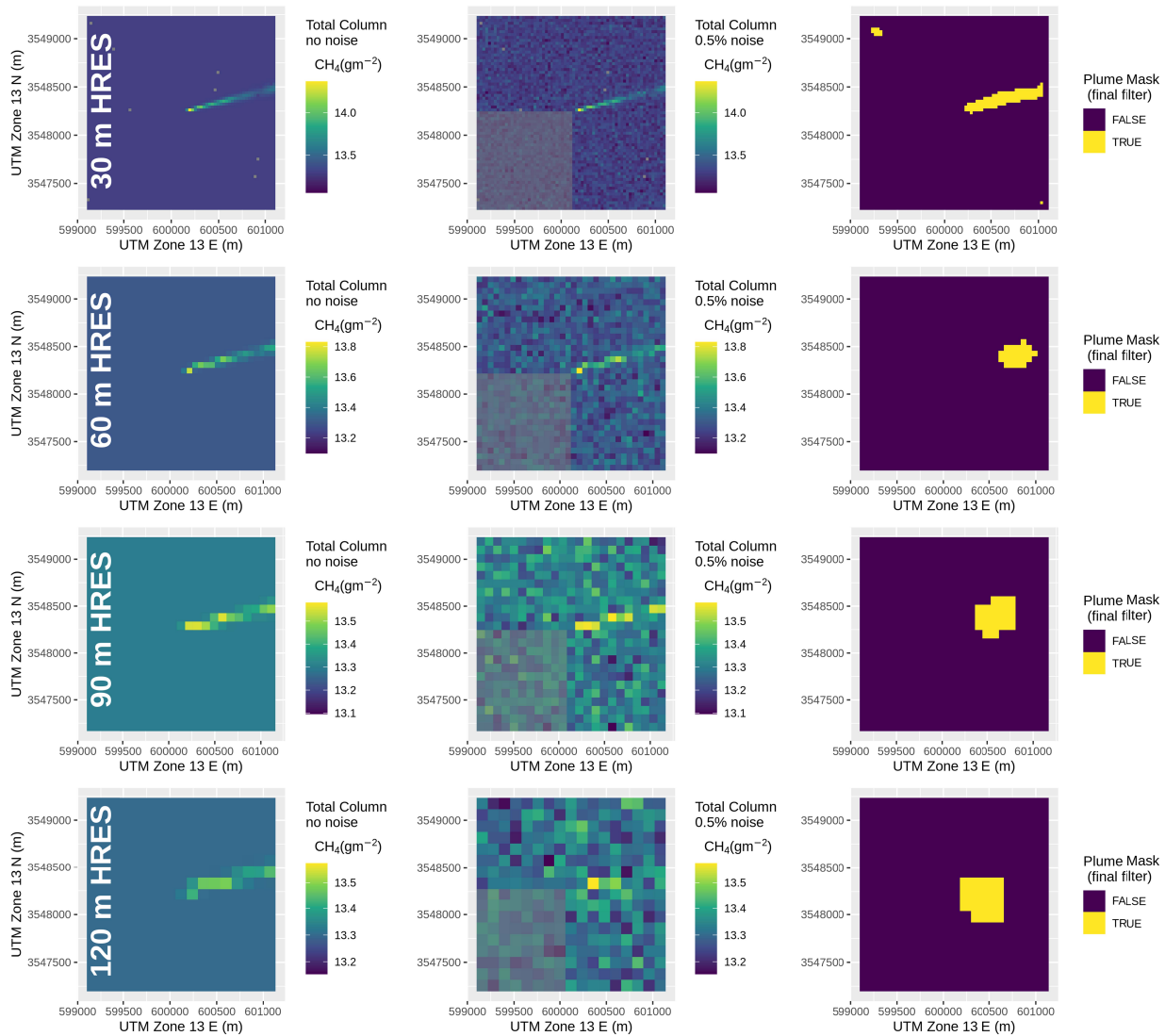


264

265 **Figure 3. Mean and 95% confidence interval of the retrieved emission rates for the 50 kg**  
 266 **hr<sup>-1</sup> continuous releases. Solid bars (left) are for 0.5% Gaussian noise in the background,**  
 267 **while the hatched bars (right) are for 1.0% Gaussian noise.**

268

269 Figure 4 shows the plume simulation and masking results for a case with  $4 \text{ m s}^{-1}$  wind  
 270 speed. The top row shows the results for the native 30 m horizontal resolution of the simulations,  
 271 corresponding to a satellite ground sample distance of 30 m. We then degraded the resolution to  
 272 60 m, 90 m, and 120 m by averaging the original 30 m pixels and then applied the plume  
 273 identification algorithm. Only at the 30 m resolution was the plume mask able to retain the shape  
 274 of the simulated plume, with the other resolution only identifying enhanced blobs 0.25 – 0.75 km  
 275 downwind from the original source. This again suggest that improvements are needed to the  
 276 plume identification algorithm, as the plume can be clearly identified by eye at 60 m resolution,  
 277 and somewhat at 90 m resolution. However, at 120 m resolution most of the plume enhancement  
 278 has been lost in the background, suggesting that even an improved plume identification  
 algorithm would not be able to identify a  $50 \text{ kg hr}^{-1}$  leak at this spatial resolution.



279

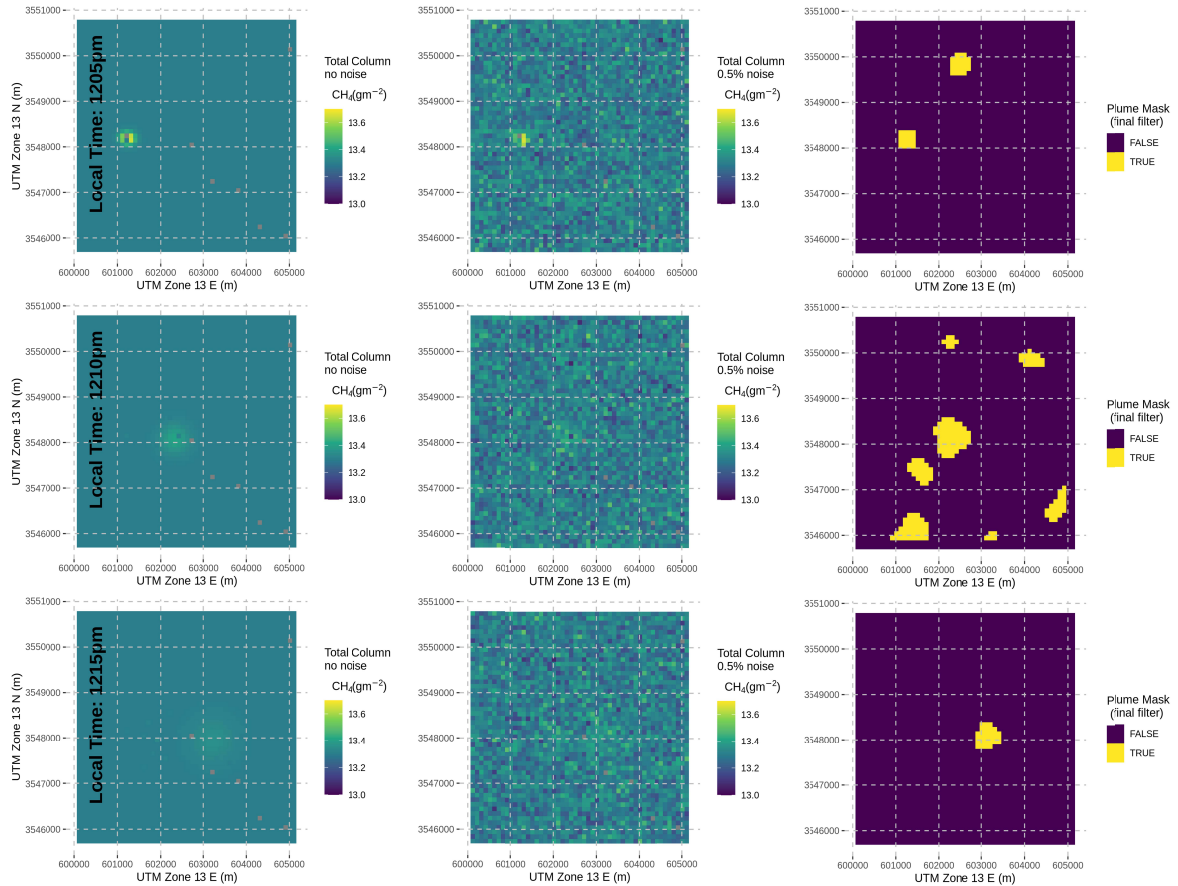
280 **Figure 4. Impact of different horizontal resolutions on the plume identification algorithm.**  
 281 **From top to bottom, the rows show the results at 30 m, 60 m, 90 m, and 120 m horizontal**  
 282 **resolution. Left column is the simulated column enhancement for the plume, middle**  
 283 **column is after a background with 0.5% noise is added, and right column is the resulting**  
 284 **plume mask. All simulations are for a release rate of  $50 \text{ kg hr}^{-1}$  and a wind speed of  $4.2 \text{ m s}^{-1}$**   
 285 **(20 UTC on March 8, 2016).**

286 3.2 Intermittent Sources

287 Figure 5 shows the results for the instantaneous release at 5 min (top row), 10 min  
 288 (middle row) and 15 min (bottom row) after release for a 0.5% noisy background. The  
 289 identification is very time dependent, as the instantaneous release results in a puff that is  
 290 dispersing along both horizontal axes, resulting in concentrations that fall off more rapidly. The

291 maximum CH<sub>4</sub> column enhancement drops from 8 g m<sup>-2</sup> at release start to 0.025 g m<sup>-2</sup> 20 minutes  
 292 downwind.

293



294 **Figure 5. Plume identification results for an instantaneous release of 33.5 kg from a**  
 295 **compressor blow-down at noon local time (UTC-7h) on March 8, 2016. From top to**  
 296 **bottom, the rows show the results for 5, 10, and 15 minutes after emission. Left column is**  
 297 **the simulated column enhancement for the plume, middle column is after a background**  
 298 **with 0.5% noise is added, and right column is the resulting plume mask.**

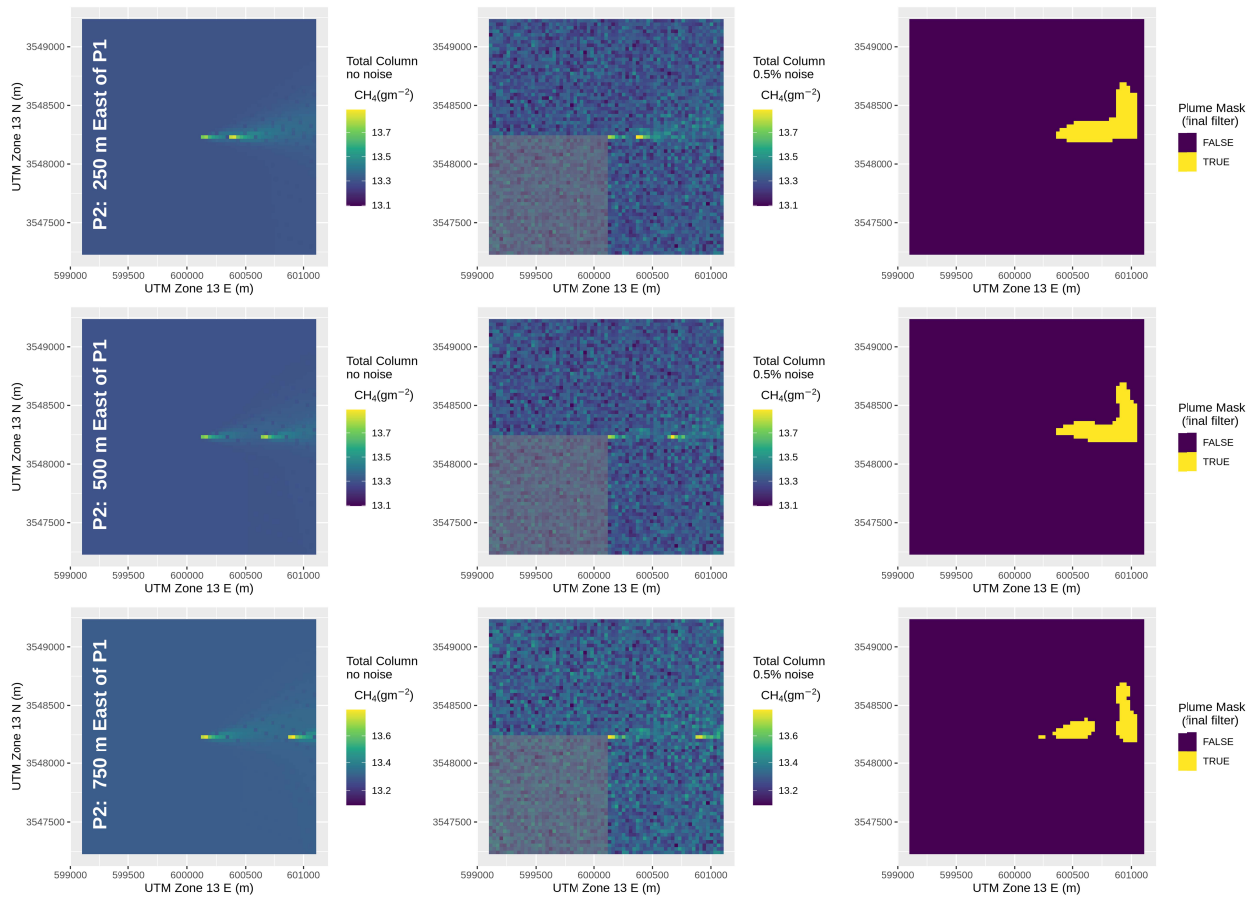
299 At 5 minutes, the puff is clearly identifiable by eye against the noisy background (Figure  
 300 5), and the plume identification algorithm successfully identifies the puff, although a spurious  
 301 plume identification is also made to the northeast. At 10 min, it becomes difficult to identify the  
 302 puff visually. While the plume identification algorithm does identify the puff location, it also  
 303 classifies a large number of background locations as plume. At 15 min, it is difficult to identify  
 304 the plume by eye, and the plume identification algorithm only identifies the central core of the  
 305 plume, and after 15 min the puff is no longer detectable. This suggests an increased probability  
 306 of detection of short duration events with higher frequency (hourly or less) observations.

### 307 3.3 Overlapping Continuous Sources

308 For cases with equal source strength of 50 kg hr<sup>-1</sup> and a background column precision of

309 0.5%, the plume identification algorithm is generally able to separate the two overlapping  
310 sources if they are 0.5 km apart or more, regardless of the wind direction, but is not able to  
311 separate them if they are only 0.25 km apart. Figure 6 shows the most challenging case, where  
312 the wind is parallel with the line connecting the sources and so the upwind plume covers the  
313 downwind one (90-degree wind rotation from the original case in Figure 2). When the sources  
314 are only 0.25 km apart (top row), the plumes are merged in the plume mask. However, at 0.5 km  
315 (middle row) and 0.75 km (bottom row), the plume identification algorithm is able to distinguish  
316 the two plumes. Note that the horizontally dispersive case chosen here likely contributes to the  
317 ability to separate these plumes, as the centerline concentrations of the upwind plume have fallen  
318 to background levels before the second source is reached. Results for winds perpendicular to the  
319 line connecting the sources (zero-degree wind rotation) and the 45-degree rotation case, are  
320 shown in Supplemental Figures S1 and S2, respectively. The perpendicular shows two separate  
321 plumes when they are spaced 0.5 km and 0.75 km apart. At 0.25 km the two plumes merge into a  
322 single feature, with a small near-source bifurcation in the plume mask being the only indication  
323 of overlapping sources.

324 If the strength of the western source is increased to  $500 \text{ kg hr}^{-1}$ , the downwind plume is  
 325 no longer separable from the upwind plume if the wind is parallel to the line connecting the  
 326 sources (Supplemental Figure S3). This is true even if the locations of the sources are reversed

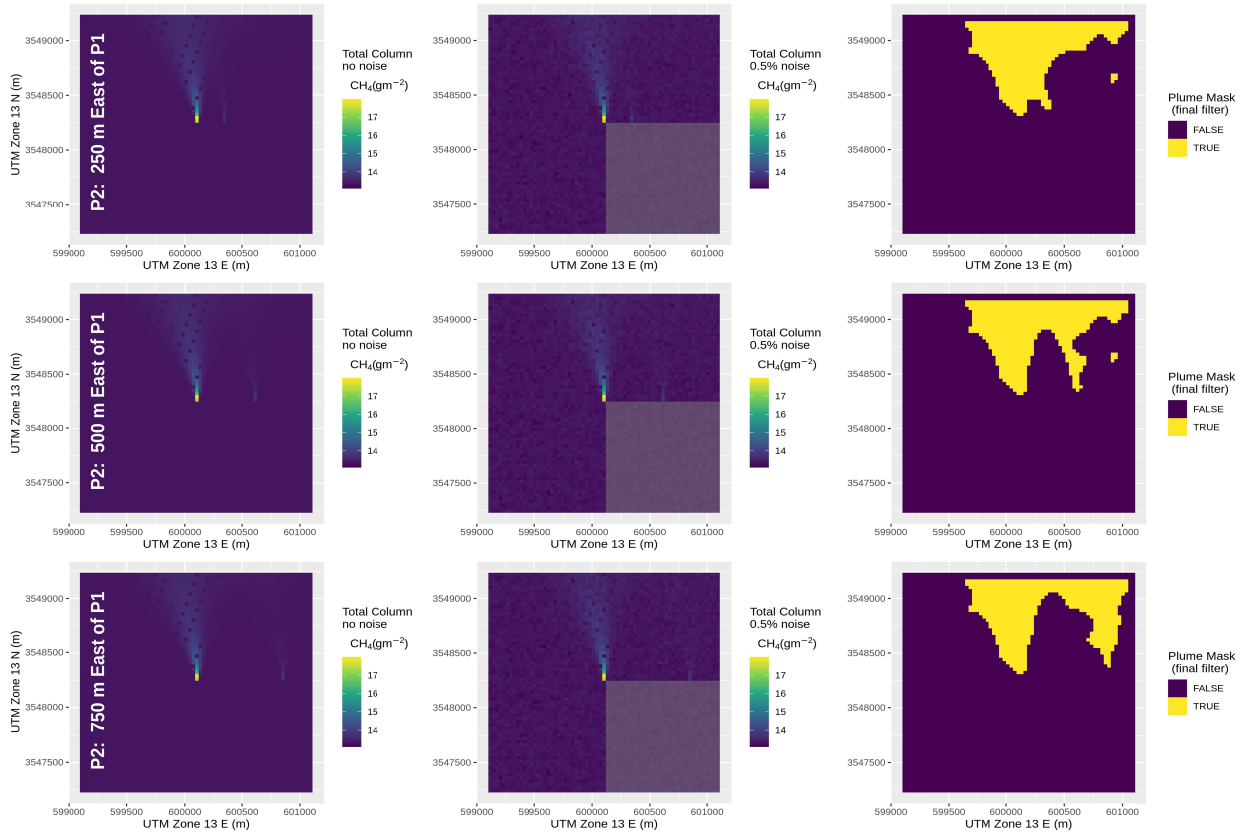


327 (not shown). Figure 7 shows the results if the wind is perpendicular. At 0.25 km, the second  
 328 source is only identifiable as a small tendril disrupting the overall symmetry of the larger plume.  
 329 At 0.5 km the tendril is more pronounced, and at 0.75 km we clearly see two distinct, if  
 330 eventually overlapping, plumes. These plumes are in principle separable, but the plume  
 331 identification algorithm would have to be refined to fully separate the two plumes. The 45-  
 332 degree rotated case (Supplemental Figure S4) gives similar results to the perpendicular case in  
 333 Figure 7.

334

335 **Figure 6. Plume identification results for two sources emitting  $50 \text{ kg hr}^{-1}$  of  $\text{CH}_4$  when the**  
 336 **winds are parallel to the line connecting the two sources. From top to bottom, the rows**  
 337 **show the results for when the sources are 0.25 km, 0.5 km, and 0.75 km apart. Left column**  
 338 **is the simulated column enhancement for the plume, middle column is after a background**  
 339 **with 0.5% noise is added, and right column is the resulting plume mask.**

340



341  
 342 **Figure 7. Plume identification results for two sources, the western one emitting 500 kg hr<sup>-1</sup>**  
 343 **of CH<sub>4</sub> and the eastern one emitting 50 kg hr<sup>-1</sup> of CH<sub>4</sub> when the winds are perpendicular to**  
 344 **the line connecting the two sources. From top to bottom, the rows show the results for when**  
 345 **the sources are 0.25 km, 0.5 km, and 0.75 km apart. Left column is the simulated column**  
 346 **enhancement for the plume, middle column is after a background with 0.5% noise is**  
 347 **added, and right column is the resulting plume mask.**  
 348

#### 349 4 Conclusions

350 To help with the development of an operationally focused satellite constellation to detect  
 351 CH<sub>4</sub> emissions for the oil and gas industry, we applied a plume identification and quantification  
 352 method based on Varon et al. (2018) to three types of sources. First, isolated continuous sources  
 353 with source strength of 50 kg hr<sup>-1</sup> were simulated as 80-90% of methane sources from oil and gas  
 354 are this size or larger. Second, an isolated instantaneous source of 33.5 kg was used to simulate  
 355 an intermittent release from a compressor blowdown. Third, overlapping continuous sources  
 356 were simulated for different distances, wind directions, and source strengths. A retrieved column  
 357 precision of 0.5%-1.0% was assumed for these cases, based on a future satellite instrument  
 358 operating in the 2050-2400 μm band with a signal to noise ratio (SNR) between 100-150 and a  
 359 spectral resolution between 1- 5 nm.

360 For the isolated continuous sources, the retrieved emissions varied between 25-200 kg hr<sup>-1</sup>  
 361 <sup>1</sup>, with the daytime cases showing a mean bias of 25-50 kg hr<sup>-1</sup>. As the plume identification  
 362 algorithm tends to be overly conservative in identifying pixels as within the plume, this positive

363 bias suggests the need for improvements in the  $U_{eff}$  parameterization used in the IME method.  
364 The plume mask performed the best at a horizontal resolution of 30-60 m, with the performance  
365 degrading significantly at horizontal resolution greater than 90 m.

366 As the instantaneous releases disperse in both horizontal directions, the CH<sub>4</sub> columns fall  
367 off as the square of distance/time downwind, rather than the linear decrease seen with continuous  
368 releases. This limits the time downwind that a puff from an instantaneous release is visible. With  
369 a 0.5% CH<sub>4</sub> column precision, a 33.5 kg CH<sub>4</sub> release is visible for 15 minutes after release. Thus,  
370 the typical compressor start-up, compressor blow-down, and liquid unloading with a plunger lift  
371 (7-200 kg, Allen et al., 2015) would have to be observed shortly after release to be detected by  
372 satellite. Liquid unloadings without plunger lifts tend to have larger releases (400-700 kg, Allen  
373 et al., 2015, Pacsi et al., 2020), and so may be visible for up to one hour after release. Thus, the  
374 releases larger than 50 kg/hr would be detected by satellite. Oil well completions tend to be a  
375 factor of 10 smaller (e.g., Cardoso-Saldaña and Allen, 2021), and so only the largest emitters  
376 would be detected.

377 Overlapping plumes of similar small source strength were difficult to separate if they  
378 were only 0.25 km apart but were separable by the plume identification algorithm if they were  
379 0.5 km apart or more. This result was independent of whether the wind was perpendicular or  
380 parallel to the line connecting the two sources. However, when one source was much larger than  
381 the other, the resulting plumes tended to merge together downwind, although the sources were  
382 generally separable near the source. This suggests that a modified plume identification algorithm  
383 could be able to better separate these plumes.

384 Future work will focus on further refinement of the plume identification algorithm to  
385 better identify the full plume and to better separate overlapping plumes from neighboring  
386 sources. Further work is also needed to separate the puffs from intermittent sources from  
387 statistical fluctuations in the retrieved background columns. In addition, improvements in the  
388 parameterization of  $U_{eff}$ , potentially incorporating additional data beyond the  $U_{10}$  wind speed,  
389 should be explored.

## 390 **Acknowledgments**

391 Funding to perform the analyses reported here was provided by ExxonMobil Upstream Research  
392 Company.

393

## 394 **Open Research**

395 V3.3 of the SCICHEM model used for the dispersion modeling studies performed in this  
396 work is publicly available at <https://github.com/epri-dev/SCICHEM/tree/3.3> from the Electric  
397 Power Research Institute. V12.13 of LBLRTM, used for calculating the Jacobians to estimate the  
398 precision of the retrieved methane columns for different assumptions of instrument resolution  
399 and SNR, is publicly available at <https://github.com/AER-RC/LBLRTM> from Verisk  
400 Atmospheric and Environmental Research. The LBLRTM license is free for all non-commercial  
401 research uses.

402 The input (meteorological and terrain) and output data (raw concentration output,  
403 calculated methane columns) from SCICHEM used in this study are available at zenodo via DOI  
404 10.5281/zenodo.7757810 under a Creative Commons Attribution 4.0 International license.  
405

## 406 References

407 Allen, D.T., Torres, V.M., Thomas, J., Sullivan, D.W., Harrison, M., Hendler, A., Herndon, S.C.,  
408 Kolb, C.E., Fraser, M.P., Hill, A.D. & Lamb, B.K. (2013), Measurements of methane emissions  
409 at natural gas production sites in the United States. *Proceedings of the National Academy of*  
410 *Sciences*, 110(44), 17768-17773. <https://doi.org/10.1073/pnas.130488011>

411 Allen, D.T., Sullivan, D.W., Zavala-Araiza, D., Pacsi, A.P., Harrison, M., Keen, K., Fraser,  
412 M.P., Daniel Hill, A., Lamb, B.K., Sawyer, R.F. & Seinfeld, J.H. (2015), Methane emissions  
413 from process equipment at natural gas production sites in the United States: Liquid unloadings.  
414 *Environmental Science & Technology*, 49(1), 641-648. <https://doi.org/10.1021/es504016r>

415 Allen, D.T., Cardoso-Saldaña, F.J. & Kimura, Y. (2017), Variability in spatially and temporally  
416 resolved emissions and hydrocarbon source fingerprints for oil and gas sources in shale gas  
417 production regions. *Environmental Science & Technology*, 51(20), 12016-12026.  
418 <https://doi.org/10.1021/acs.est.7b02202><https://doi.org/10.1021/acs.est.7b02202>

419 Alvarado, M.J., Payne, V.H., Mlawer, E.J., Uymin, G., Shephard, M.W., Cady-Pereira, K.E.,  
420 Delamere, J.S. & Moncet, J.L. (2013), Performance of the Line-By-Line Radiative Transfer  
421 Model (LBLRTM) for temperature, water vapor, and trace gas retrievals: recent updates  
422 evaluated with IASI case studies. *Atmospheric Chemistry and Physics*, 13(14), 6687-6711.  
423 <https://doi.org/10.5194/acp-13-6687-2013>

424 Brandt, A.R., Heath, G.A. & Cooley, D. (2016), Methane leaks from natural gas systems follow  
425 extreme distributions. *Environmental Science & Technology*, 50(22), 12512-12520.  
426 <http://dx.doi.org/10.1021/acs.est.6b04303>

427 Cardoso-Saldaña, F.J. & Allen, D.T. (2021), Projecting the temporal evolution of methane  
428 emissions from oil and gas production basins. *Environmental Science & Technology*, 55,  
429 2811–2819. <https://doi.org/10.1021/acs.est.0c04224>

430 Cardoso-Saldaña, F.J. (2022), Tiered Leak Detection and Repair Programs at Oil and Gas  
431 Production Facilities. Preprint at chemrxiv.org, version 1. doi:[10.26434/chemrxiv-2022-](https://doi.org/10.26434/chemrxiv-2022-f7dfv)  
432 [f7dfv](https://doi.org/10.26434/chemrxiv-2022-f7dfv)doi:[10.26434/chemrxiv-2022-f7dfv](https://doi.org/10.26434/chemrxiv-2022-f7dfv)

433 Chen, Y., Sherwin, E.D., Berman, E.S., Jones, B.B., Gordon, M.P., Wetherley, E.B., Kort, E.A.  
434 & Brandt, A.R. (2022), Quantifying Regional Methane Emissions in the New Mexico Permian  
435 Basin with a Comprehensive Aerial Survey. *Environmental Science & Technology*, 56(7), 4317-  
436 4323. <https://doi.org/10.1021/acs.est.1c06458>

444

- 445 Clough, S.A., Shephard, M.W., Mlawer, E.J., Delamere, J.S., Iacono, M.J., Cady-Pereira, K.,  
446 Boukabara, S. & Brown, P.D. (2005), Atmospheric radiative transfer modeling: A summary of  
447 the AER codes. *Journal of Quantitative Spectroscopy and Radiative Transfer*, 91(2), 233-244.  
448 <https://doi.org/10.1016/j.jqsrt.2004.05.058>  
449
- 450 Cusworth, D.H., Jacob, D.J., Sheng, J.X., Benmergui, J., Turner, A.J., Brandman, J., White, L. &  
451 Randles, C.A. (2018), Detecting high-emitting methane sources in oil/gas fields using satellite  
452 observations. *Atmospheric Chemistry and Physics*, 18(23), 16885-16896.  
453 <https://doi.org/10.5194/acp-18-16885-2018>  
454
- 455 Cusworth, D.H., Jacob, D.J., Varon, D.J., Chan Miller, C., Liu, X., Chance, K., Thorpe, A.K.,  
456 Duren, R.M., Miller, C.E., Thompson, D.R. & Frankenberg, C. (2019), Potential of next-  
457 generation imaging spectrometers to detect and quantify methane point sources from space.  
458 *Atmospheric Measurement Techniques*, 12(10), 5655-5668. [https://doi.org/10.5194/amt-12-5655-](https://doi.org/10.5194/amt-12-5655-2019)  
459 [2019](https://doi.org/10.5194/amt-12-5655-2019)  
460
- 461 Cusworth, D.H., Duren, R.M., Thorpe, A.K., Tseng, E., Thompson, D., Guha, A., Newman, S.,  
462 Foster, K.T. & Miller, C.E. (2020), Using remote sensing to detect, validate, and quantify  
463 methane emissions from California solid waste operations. *Environmental Research Letters*,  
464 15(5), 054012. doi:10.1088/1748-9326/ab7b99  
465
- 466 Cusworth, D.H., Duren, R.M., Thorpe, A.K., Olson-Duvall, W., Heckler, J., Chapman, J.W.,  
467 Eastwood, M.L., Helmlinger, M.C., Green, R.O., Asner, G.P. & Dennison, P.E. (2021),  
468 Intermittency of large methane emitters in the Permian Basin. *Environmental Science &*  
469 *Technology Letters*, 8(7), 567-573. <https://doi.org/10.1021/acs.estlett.1c00173>  
470
- 471 Cusworth, D.H., Thorpe, A.K., Ayasse, A.K., Stepp, D., Heckler, J., Asner, G.P., Miller, C.E.,  
472 Yadav, V., Chapman, J.W., Eastwood, M.L. & Green, R.O. (2022), Strong methane point  
473 sources contribute a disproportionate fraction of total emissions across multiple basins in the  
474 United States. *Proceedings of the National Academy of Sciences*, 119(38), e2202338119.  
475 <https://doi.org/10.1073/pnas.2202338119>  
476
- 477 Duren, R.M., Thorpe, A.K., Foster, K.T., Rafiq, T., Hopkins, F.M., Yadav, V., Bue, B.D.,  
478 Thompson, D.R., Conley, S., Colombi, N.K. & Frankenberg, C. (2019), California's methane  
479 super-emitters. *Nature*, 575(7781), 180-184. <https://doi.org/10.1038/s41586-019-1720-3>  
480
- 481 Ehret, T., De Truchis, A., Mazzolini, M., Morel, J.M., D'asprenmont, A., Lauvaux, T., Duren, R.,  
482 Cusworth, D. & Facciolo, G. (2022), Global tracking and quantification of oil and gas methane  
483 emissions from recurrent Sentinel-2 imagery. *Environmental Science & Technology*, 56(14),  
484 10517-10529. <https://doi.org/10.1021/acs.est.1c08575>  
485
- 486 Jacob, D. J., Varon, D. J., Cusworth, D. H., Dennison, P. E., Frankenberg, C., Gautam, R.,  
487 Guanter, L., Kelley, J., McKeever, J., Ott, L. E., Poulter, B., Qu, Z., Thorpe, A. K., Worden, J.  
488 R., & Duren, R. M. (2022), Quantifying methane emissions from the global scale down to point  
489 sources using satellite observations of atmospheric methane. *Atmospheric Chemistry and*  
490 *Physics*, 22, 9617–9646. <https://doi.org/10.5194/acp-22-9617-2022>

- 491  
492 Jongaramrungruang, S., Frankenberg, C., Matheou, G., Thorpe, A.K., Thompson, D.R., Kuai, L.  
493 & Duren, R.M. (2019), Towards accurate methane point-source quantification from high-  
494 resolution 2-D plume imagery. *Atmospheric Measurement Techniques*, 12(12), 6667-6681.  
495 <https://doi.org/10.5194/amt-12-6667-2019>  
496
- 497 Lauvaux, T., Giron, C., Mazzolini, M., d'Aspremont, A., Duren, R., Cusworth, D., Shindell, D.  
498 & Ciais, P. (2022), Global assessment of oil and gas methane ultra-emitters. *Science*, 375(6580),  
499 557-561. DOI: 10.1126/science.abj4351 DOI: 10.1126/science.abj4351  
500
- 501 Nisbet, E.G., Fisher, R.E., Lowry, D., France, J.L., Allen, G., Bakkaloglu, S., Broderick, T.J.,  
502 Cain, M., Coleman, M., Fernandez, J. & Forster, G. (2020), Methane mitigation: methods to  
503 reduce emissions, on the path to the Paris agreement. *Reviews of Geophysics*, 58(1),  
504 e2019RG000675. <https://doi.org/10.1029/2019RG000675>  
505
- 506 Pacsi, A., Sullivan, D.W. & Allen, D.T. (2020), Revised Estimation Method for Emissions from  
507 Automated Plunger Lift Liquid Unloadings. *Environments*, 7(4), 25.  
508 <https://doi.org/10.3390/environments7040025>  
509
- 510 Pernini, T.G., Zaccheo, T.S., Dobler, J. & Blume, N. (2022), Estimating oil sands emissions  
511 using horizontal path-integrated column measurements. *Atmospheric Measurement Techniques*,  
512 15(2), 225-240. <https://doi.org/10.5194/amt-15-225-2022>  
513
- 514 Sánchez-García, E., Gorroño, J., Irakulis-Loitxate, I., Varon, D.J. & Guanter, L. (2022),  
515 Mapping methane plumes at very high spatial resolution with the WorldView-3 satellite.  
516 *Atmospheric Measurement Techniques*, 15(6), 1657-1674. [https://doi.org/10.5194/amt-15-1657-  
517 2022](https://doi.org/10.5194/amt-15-1657-2022)  
518
- 519 Saunio, M., Stavert, A.R., Poulter, B., Bousquet, P., Canadell, J.G., Jackson, R.B., Raymond,  
520 P.A., Dlugokencky, E.J., Houweling, S., Patra, P.K. & Ciais, P. (2020), The global methane  
521 budget 2000–2017. *Earth System Science Data*, 12(3), 1561-1623. [https://doi.org/10.5194/essd-  
522 12-1561-2020](https://doi.org/10.5194/essd-12-1561-2020)  
523
- 524 Szopa, S., V. Naik, B. Adhikary, P. Artaxo, T. Berntsen, W.D. Collins, S. Fuzzi, L. Gallardo, A.  
525 Kiendler-Scharr, Z. Klimont, H. Liao, N. Unger, & P. Zanis (2021), Short-Lived Climate  
526 Forcers. In *Climate Change 2021: The Physical Science Basis. Contribution of Working Group I  
527 to the Sixth Assessment Report of the Intergovernmental Panel on Climate Change* [Masson-  
528 Delmotte, V., P. Zhai, A. Pirani, S.L. Connors, C. Péan, S. Berger, N. Caud, Y. Chen, L.  
529 Goldfarb, M.I. Gomis, M. Huang, K. Leitzell, E. Lonnoy, J.B.R. Matthews, T.K. Maycock, T.  
530 Waterfield, O. Yelekçi, R. Yu, & B. Zhou (eds.)]. Cambridge University Press, Cambridge,  
531 United Kingdom and New York, NY, USA, 817–922. doi:10.1017/9781009157896.008  
532
- 533 United States Environmental Protection Agency (2021), Standards of Performance for New,  
534 Reconstructed, and Modified Sources and Emissions dssdfgsdgd for Existing Sources: Oil and  
535 Natural Gas Sector Climate Review, 86 Fed. Reg. 63,110 (Nov. 15, 2021).  
536

- 537 Varon, D.J., Jacob, D.J., McKeever, J., Jervis, D., Durak, B.O., Xia, Y. & Huang, Y. (2018),  
538 Quantifying methane point sources from fine-scale satellite observations of atmospheric methane  
539 plumes. *Atmospheric Measurement Techniques*, 11(10), 5673-5686. [https://doi.org/10.5194/amt-  
540 11-5673-2018](https://doi.org/10.5194/amt-11-5673-2018)
- 541  
542 Varon, D.J., Jacob, D.J., Jervis, D. & McKeever, J. (2020), Quantifying time-averaged methane  
543 emissions from individual coal mine vents with GHGSat-D satellite observations. *Environmental  
544 Science & Technology*, 54(16), 10246-10253. <https://doi.org/10.1021/acs.est.0c01213>  
545
- 546 Varon, D.J., Jervis, D., McKeever, J., Spence, I., Gains, D. & Jacob, D.J. (2021), High-frequency  
547 monitoring of anomalous methane point sources with multispectral Sentinel-2 satellite  
548 observations. *Atmospheric Measurement Techniques*, 14(4), 2771-2785.  
549 <https://doi.org/10.5194/amt-14-2771-2021>  
550
- 551 Varon, D.J., Jacob, D.J., Sulprizio, M., Estrada, L.A., Downs, W.B., Shen, L., Hancock, S.E.,  
552 Nesser, H., Qu, Z., Penn, E. & Chen, Z. (2022), Integrated Methane Inversion (IMI 1.0): a user-  
553 friendly, cloud-based facility for inferring high-resolution methane emissions from TROPOMI  
554 satellite observations. *Geoscientific Model Development*, 15(14), 5787-5805.  
555 <https://doi.org/10.5194/gmd-15-5787-2022>  
556
- 557 Zimmerle, D., Duggan, G., Vaughn, T., Bell, C., Lute, C., Bennett, K., Kimura, Y., Cardoso-  
558 Saldaña, F.J. & Allen, D.T. (2022), Modeling air emissions from complex facilities at detailed  
559 temporal and spatial resolution: The Methane Emission Estimation Tool (MEET). *Science of The  
560 Total Environment*, 824, 153653. <https://doi.org/10.1016/j.scitotenv.2022.153653>  
561